Vortex-induced vibration for an isolated circular cylinder under the wake interference of an oscillating airfoil: Part II. Single degree of freedom

G.Q ZHANG[1,2*], L.C JI[1] and X Hu[1]

[1]Key Laboratory of Dynamics and Control of Flight Vehicle, Ministry of Education, Beijing Institute of Technology, Beijing, China 100081

[2]Aerospace Engineering Division, School of Mechanical and Aerospace Engineering, Nanyang Technological University, Singapore 639798

[*]Corresponding author: zhanggq@bit.edu.cn

Abstract

The vortex-induced vibration behind an isolated cylinder under the wake interference of an oscillating airfoil at different oscillating frequencies and amplitudes have been studied numerically. Our previous research mainly focused on the two degree of freedom vibration problem, several types of the phase portraits of the displacement have been newly found, including the "half -8" and "cone-net" types as reduced velocity increases. At present, we have continued the research to the single degree of freedom vibration, the corresponding results had been found that under the wake of the free steady flow, as the reduced velocity increases, the phase portraits displacements of the single degree of freedom vibrating cylinder will begin to rotate counterclockwise from the first and third quadrants to the second and fourth quadrants in a Cartesian coordinate system. Under the wake of the oscillating airfoil, the single bending curve and the single closed orbit (double "8-shape" like) of the displacements are newly found in the drag and thrust producing cases respectively. Except this, the two triplets of vortices have also been newly found in the pair and single plus pair wakes at each cycle. The vorticity dynamics behind the vibrating cylinder together with the corresponding force variations have also been obtained computationally and analyzed in details.

Abbreviations

A,Oscillating amplitude (*m*); A_D,dimensionless amplitude of airfoil ($A_D = 2A/L$); *c*,damping of the system (*N·s/m*); $C_{D,}$Drag coefficient; *D*,Diameter of cylinder (*m*); $C_{L,}$Lift coefficient; *F*,vortex-induced coupling force (*N*); *Re*,Reynold number ($\mathrm{Re} = LU/\nu$); *k*,stiffness of the spring (*N/m*); $St_{D,}$width-based Strouhal number ($St_D = fL/U$); *L*,width of airfoil (*m*); *Vr*,Reduced velocity (*Vr=U/(f_N D)*; *m*,mass of the cylinder (*kg*); υ ,kinematic viscosity of the fluid ($cm^2 s^{-1}$); *P*,static pressure (*Pa*); ξ,non-dimensional damping coefficient; *Q*,center position of the cylinder (*m*); "*P*",a pair of vortices; *t*,flow time (*s*); *"S"*,single vortex; *U*,free stream velocity (*m/s*); *VIV*,vortex induced vibration; *f*,oscillating frequency of airfoil (s^{-1}); *DOF*,degree of freedom; f_{so} ,vortex-shedding frequency (cylinder); *X* ,Y,nodes in the streamwise/ transverse direction; f_N ,natural frequency (cylinder); *i, j*,nodes on the whole edge of airfoil /cylinder

Keywords: Vortex shedding; Vortex-induced-vibration; Cylinder; Airfoil; Oscillating

Introduction

In nature, fish and cetaceans employ their oscillating tails, which are closely resembled of a high-aspect-ratio airfoil, to produce propulsive and maneuvering forces during swimming. Insight into the vortex formation and shedding are important in order to understand the underling physical phenomena of these processes. A number of experimental and numerical studies were carried out due to its significance in practical engineering applications, for example, the reduction of aerodynamic loads on cylindrical structures, suppression of vortex-induced vibration of offshore risers and flow energy harvest etc.[1-3]. So the formation and shedding of the wake behind an oscillating airfoil had drawn more and more attention, which were always found to include the von Kármán type in which two vortices of opposite sign are shedded per oscillation cycle (referred to as “2S”) and wakes in which two vortex pairs are shedded per oscillation cycle (referred to as “2P”). Lu et al.[4] had conducted the simulation for the fluid flow over a rotationally oscillating circular cylinder with splitter plate. The corresponding results had revealed that the phenomenon of rotation bifurcation, i.e., the equilibrium position of the rotary oscillation deflects to a position which is not parallel to the free stream, is found to only occur at higher

reduced velocities. The longer splitter plate has the lower critical reduced velocity. The occurrence of bifurcation is attributed to the anti-symmetry breaking of the wake flow evolution. Hsieh[5] had also conducted the experiment to present the vibration amplitude and oscillation frequency for different reduced velocities, the mean velocity field, turbulence characteristics, vortex behavior, gap flow velocity, and normal/shear stresses on the boundary were measured/calculated, leading to new insights on the flow field behavior. Schnipper et al.[6] presented the experimental study of a symmetrical airfoil performing oscillating oscillations in a vertically flowing soap film. The wake types in a phase diagram based on the width-based Strouhal number and the dimensionless amplitude were constructed. The results highlighted the essential features of the vortex formation process which could be used to describe a number of characteristics of the phase diagram using simple analytical arguments.

Vortex induced vibration (VIV) for elastically mounted obstacle occurs when the vortex-shedding frequency and the obstacles natural frequency are closely matched, which can be found in many practical engineering applications. In addition to their great practical relevance, VIV problems are also important from a fundamental standpoint due to the enormous richness of their underlying vorticity dynamics. A circular cylinder has a tendency to vibrate when it is subjected to a steady flow. The vibration can be either the single degree of freedom (1-DOF) or the multiple degrees of freedom (x-DOF). Once the vibration begins, the flow field behind the cylinder will become vastly different from that of the fixed cylinder. This vibration can affect the time-dependent pressure and shear stress distributions (Al-Jamal and Dalton[7]). Prediction of this self-excited vibration has gradually become a challenge to fluid mechanists and offshore designers.

It is well known that the flow past a single cylinder can serve as the generic VIV model problem and has been widely studied both numerically and experimentally for example, Williamson and Govardhan[8], Borazjani[9] and Sarpkaya[10]. However, even this relatively simple system exhibits enormous complexity. The complexity of VIV dynamics of a single elastic mounted cylinder is expected to increase considerably when it is introduced into the oscillating airfoil. Large eddy simulation (LES) method for steady flow past a stationary circular is thought to be a better calculation method at high Reynolds numbers than the direct numerical simulation (DNS) method (Al-Jamal and Dalton[7]).

Our previous research mainly focused on the 2-DOF VIV problems[11], The “2S” and “P+S” mode are found in the drag-producing von Kármán vortex wake and thrust-producing inverted von Kármán vortex wake, respectively. For the “2P” case, the pairs of vortices with different sizes are laterally parallel to each other. For the “2P+2S” case, the merged single vortices do not appear between the vortex pairs, but they only emerge after every two pairs of vortices. For 2-DOF VIV in the wake of the steady flow, seven types of the phase portraits of the displacement shapes have been newly found, including the "half -8” and "cone-net" types as reduced velocity increases.

Based on these, we have conducted the further research on the single degree of freedom problem. There are two main objectives in our present study, (1) Investigation on the 1-DOF VIV for a single elastically mounted cylinder under steady flow and the wake of an oscillating airfoil (with different oscillating frequencies and amplitudes) respectively. (2) Comparison of the vortex formation and shedding patterns with different cases, i.e. i) a single oscillating airfoil case, ii) a fixed cylinder under steady flow and the wake of oscillating airfoil, and iii) a vibrating cylinder (1-DOF) under steady flow and the wake of oscillating airfoil.

The paper is organized as follows. Section II describes the governing equations including a brief description of the FSI numerical algorithm. The validation method and results are be presented and discussed in section III. Section IV discusses the vortex formation and shedding process behind the oscillating airfoil and behind the cylinder under the wake interference of the oscillating airfoil at different frequencies and amplitudes. Section V covers the 1-DOF VIV study for a single elastically mounted cylinder under steady flow and the wake of the oscillating airfoil. The vorticity dynamics behind the vibrating cylinder have also been considered. The paper will end with brief concluding remarks.

2. Governing equations and numerical method

2.1 Oscillating motion of the airfoil

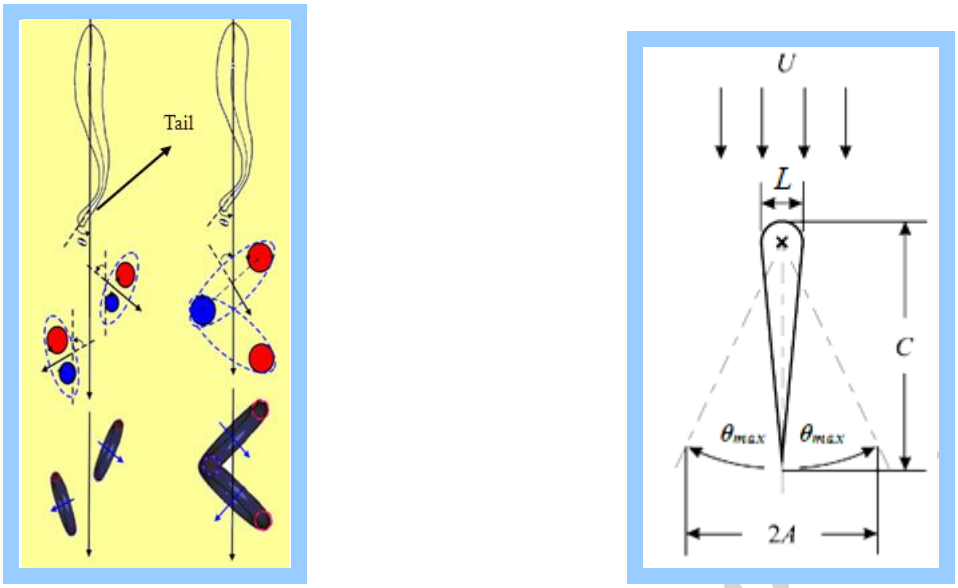

(a) The swimming fish tail (Wen et al. (2012)) (b) The motion for the oscillating airfoil

Fig.1 Schematic illustrations of the swimming fish tail and the oscillating airfoil

Fig.1(a) has shown the vortex generation mechanism for the swimming fish tail (Wen et al. (2012)[12], the two pair of vortices named “2P” and single alternating vortices named “2S” could be generated by the different oscillating frequencies and amplitudes respectively.

An airfoil with a round leading edge and a sharp trailing edge (See in Fig.1(b)) still has been adopted in the current research which has been described in details in our previous research[11]. The structure is similar to that in the experiment conducted by Godoy et al.[13] and simulation conducted by Dynnikov et al.[14]. Here, only a brief outline of the governing equations is given. unsteady incompressible Navier-Stokes equations, and some auxiliary moving and computational equations are summarized in this section.

The airfoil is driven by simple harmonic oscillation. There are three typical dimensionless parameters that can be varied so as to determine the shape of vortex shedding behind the oscillating airfoil, i.e., the width-based Strouhal number, $St_D = fL/U$, the dimensionless amplitude, $A_D = 2A/L$, and the Reynolds number, $\mathrm{Re} = LU/\nu$, where L is the width of airfoil, f is the frequency of the oscillation, U is the free stream velocity, A is the flapping amplitude and ν

is the Kinematic viscosity of the fluid (at about $0.01\,cm^2s^{-1}$). The oscillating motion can be defined simply as:

$$\theta(t) = \theta_{\max} \sin(2\pi ft) \tag{2.1}$$

2.2 Fluid flow equations and VIV of an isolated cylinder

The flow of an incompressible, viscous, Newtonian fluid in a domain will contain the rigid and elastically mounted cylinder that can free to vibrate in response to flow-induced forces generated by the free flow or the front oscillating airfoil. The fluid flow is governed by the unsteady incompressible Navier-Stokes equations, which can be written in the following Arbitrary Lagrange-Euler (ALE) formulation:

$$\frac{\partial u_i}{\partial x_i} = 0 \tag{2.2}$$

$$\frac{Du_i}{Dt} + c_j \frac{\partial u_i}{\partial x_j} = -\frac{\partial P}{\partial x_i} + \frac{1}{\mathrm{Re}} \frac{\partial}{\partial x_j}\left(\frac{\partial u_i}{\partial x_j}\right) \tag{2.3}$$

where u_i stand for the fluid velocity component along the Cartesian coordinate x_i direction. P and t denote the pressure and time respectively. Re stand for the Reynolds number based on the diameter of the cylinder D, the approach flow velocity U as well as the kinematic viscosity of the fluid υ. the convection term in Navier-Stokes equations can be modified in order to accommodate the moving boundary conditions as follows:

$$c_j = u_j - m_j \tag{2.4}$$

where m_j is the velocity components of the moving mesh occupied by the fluid.

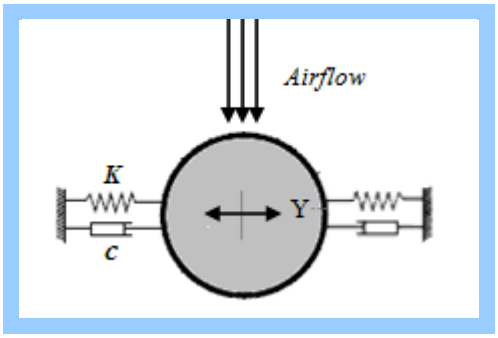

Fig.2 Arrangement of spring-damper-mass system

It is assumed that circular cylinder is mounted as a spring-damper-mass system as shown in Fig.2. It can be free to vibrate in response to flow-induced forces. The equation of motion of an elastically mounted cylinder is obtained from Newton's second law of motion that can be described by:

$$m\frac{\partial^2 Q_i}{\partial t^2}+c\frac{\partial Q_i}{\partial t}+kQ_i=F_i \tag{2.5}$$

where m is the mass of the cylinder; Q_i is the i th component of the position vector of the center of the cylinder; c is the damping of the system; k is the stiffness of the spring; and F_i is the i th component of the force imparted by the flow on the cylinder. The natural frequency f_n and non-dimensional damping coefficient ζ can be normalized using the diameter D and the free stream velocity U as follows:

$$\phi_i=\frac{Q_i}{D},\quad \tau=\frac{tU}{D},\quad \frac{\partial Q_i}{\partial t}=U\frac{\partial \phi_i}{\partial \tau},\quad \frac{\partial^2 Q_i}{\partial t^2}=\frac{U^2}{D}\frac{\partial \phi_i}{\partial \tau},\quad V_r=\frac{U}{f_n D},$$

$$m^*=\frac{4m}{\rho\pi D^2},\ \zeta=\frac{c}{2\sqrt{km}},\ f_n=\frac{1}{2\pi}\sqrt{\frac{k}{m}}. \tag{2.6}$$

The non-dimensional force coefficient (C_D and C_L) is

$$C_i = \frac{F_i}{1/2\,\rho U^2 D}$$

(2.7)

Hence, the nondimensional vibration equation in the i th direction for the cylinder can be written as follows:

$$\frac{\partial^2 \phi_i}{\partial \tau^2} + \frac{4\pi\zeta}{V_r}\frac{\partial \phi_i}{\partial \tau} + \frac{4\pi^2}{V_r{}^2}\phi_i = \frac{2C_i}{\pi m^*}$$

(2.8)

Therefore, solving Eq. 2.8 can obtain the dynamic response of the cylinder due to the VIV motion. Based on the Eq. 2.2 and 2.3, the nodal coordinates inside the ALE region (assuming the region is linear elastic) can be updated to accommodate the motion of the vibrating cylinder. So the ALE Cartesian coordinates can be solved by $\Delta\bar{\phi}_i = 0$, where $\bar{\phi}_i$ represent the horizontal and vertical coordinates after the ALE grid update, respectively.

2.3 Solution process of the fluid-structure interaction (FSI)

As our previous study has referred[11], the standard finite element method still has been adopted to generate the solution of Navier-Stokes equations. In order to consider the moving boundary conditions, the corresponding momentum equation can be discretized as follows:

$$\frac{u_i^{n+1/3} - u_i^n}{\Delta t/3} = -c_j^n \frac{\partial u_i^n}{\partial x_j} - \frac{\partial P^n}{\partial x_i} + \frac{1}{\mathrm{Re}}\frac{\partial}{\partial x_j}\left(\frac{\partial u_i^n}{\partial x_j}\right) \tag{2.9}$$

$$\frac{u_i^{n+1/2} - u_i^n}{\Delta t/2} = -c_j^{n+1/3} \frac{\partial u_i^{n+1/3}}{\partial x_j} - \frac{\partial P^n}{\partial x_i} + \frac{1}{\mathrm{Re}}\frac{\partial}{\partial x_j}\left(\frac{\partial u_i^{n+1/3}}{\partial x_j}\right) \tag{2.10}$$

$$\frac{u_i^{n+1} - u_i^n}{\Delta t} = -c_j^{n+1/2} \frac{\partial u_i^{n+1/2}}{\partial x_j} - \frac{\partial P^{n+1}}{\partial x_i} + \frac{1}{\mathrm{Re}}\frac{\partial}{\partial x_j}\left(\frac{\partial u_i^{n+1/2}}{\partial x_j}\right) \tag{2.11}$$

where the superscripts $n, n+1/3, n+1/2$ and $n+1$ stand for the time levels at $n\Delta t$, $n\Delta t+\Delta t/3$, $n\Delta t+\Delta t/2$ and $(n+1)\Delta t$, respectively. The Poisson-type pressure equation can be obtained as:

$$\frac{\partial}{\partial x_i}\left(\frac{\partial p^{n+1}}{\partial x_i}\right)=\frac{1}{\Delta t}\frac{\partial u_i^n}{\partial x_i}-\frac{\partial}{\partial x_i}\left(c_j^{n+1/2}\frac{\partial u_i^{n+1/2}}{\partial x_j}\right)+\frac{\partial}{\partial x_i}\left[\frac{1}{\mathrm{Re}}\frac{\partial}{\partial x_j}\left(\frac{\partial u_i^{n+1/2}}{\partial x_j}\right)\right] \tag{2.12}$$

Based on the above description of the velocity and pressure in Navier-Stokes equations, the present two dimensional VIV can be summarized as following steps: 1) Solving the momentum equation (Eq. 2.9) to obtain the intermediate velocity $u_i^{n+1/3}$; 2) Calculating the velocity $u_i^{n+1/2}$ based on Eq.2.10 with the available $u_i^{n+1/3}$, m_j^n and p^n ; 3) Solving the Eq. 2.12 to obtain the distribution of pressure at n+1 time level; 4) Correcting the fluid velocity based on Eq. 2.10 and getting the final u_i^{n+1}; 5) Calculating the structural response with the obtained external force; 6) Updating the computational meshes and getting the grid velocities for the next time step. The time-dependent drag and lift coefficients can be calculated by the integration operation of the instantaneous pressure and vorticity along the cylinder surface:

$$C_D(t)=-\int_0^{2\pi}p(t)\cos\theta d\theta-\frac{1}{\mathrm{Re}}\int_0^{2\pi}\omega(t)\sin\theta d\theta \tag{2.13}$$

$$C_L(t)=-\int_0^{2\pi}p(t)\sin\theta d\theta-\frac{1}{\mathrm{Re}}\int_0^{2\pi}\omega(t)\cos\theta d\theta \tag{2.14}$$

where θ is the angle from the positive x axis and $\omega(t)=\partial v/\partial x-\partial u/\partial y$ is the local vorticity.

The fluid-structure interaction (FSI) system is solved by loosely coupled method (LC-FSI), and the unsteady flow field is solved based on a finite element method with a Pressure-Based algorithm. Finite element form of the structural vortex-induced coupling vibration equations (i.e., Eq. 2.5) can be written as[11]:

$$[M]\{\ddot{Q}_i\}+[C]\{\dot{Q}_i\}+[K]\{Q_i\}=[F] \tag{2.15}$$

where, $[M]$ is the generalized consistent mass matrix of the structure; $[C]$ is the damping matrix; $[K]$ is stiffness matrix; $[F]$ is vortex-induced coupling force vector. $\{Q_i\}$, $\{\dot{Q}_i\}$ and $\{\ddot{Q}_i\}$ represents for the displacement vector, velocity vector and acceleration vector of the structure, respectively. The response value at t_{i+1} should fulfill the following dynamic equilibrium equation.

$$[M]\{\ddot{Q}_i\}_{i+1} + [C]\{\dot{Q}_i\}_{i+1} + [K]\{Q_i\}_{i+1} = [F]_{i+1} \tag{2.16}$$

In order to find the relationship between t_i and t_{i+1}, assuming the acceleration is a constant vector $\{\ddot{Q}_i\}$, which is between $\{\ddot{Q}_i\}_i$ and $\{\ddot{Q}_i\}_{i+1}$,

$$\{\ddot{Q}_i\} = \{\ddot{Q}_i\}_i + \delta\left(\{\ddot{Q}_i\}_{i+1} - \{\ddot{Q}_i\}_i\right) = \delta\{\ddot{Q}_i\}_{i+1} + (1-\delta)\{\ddot{Q}_i\}_i \tag{2.17}$$

where $0 \le \delta \le 1$, Eq.(2.17) can also be written by using another controlling parameter β. For $0 \le \beta \le 0.5$,

$$\{\ddot{Q}_i\} = \{\ddot{Q}_i\}_i + 2\beta\left(\{\ddot{Q}_i\}_{i+1} - \{\ddot{Q}_i\}_i\right) = 2\beta\{\ddot{Q}_i\}_{i+1} + (1-2\beta)\{\ddot{Q}_i\}_i \tag{2.18}$$

The velocity and displacement at t_{i+1} can be calculated by the data obtained at t_i,

$$\{\dot{Q}_i\}_{i+1} = \{\dot{Q}_i\}_i + \Delta t\{\ddot{Q}_i\}_i \tag{2.19}$$

and

$$\{Q_i\}_{i+1} = \{Q_i\}_i + \Delta t\{\dot{Q}_i\}_i + \frac{1}{2}\Delta t^2\{\ddot{Q}_i\}_i \tag{2.20}$$

Substituting Eqs. (2.17) and (2.18) into Eqs.(2.19) and (2.20) respectively, they become

$$\{\dot{Q}_i\}_{i+1} = \{\dot{Q}_i\}_i + \left[(1-\delta)\{\ddot{Q}_i\}_i + \delta\{\ddot{Q}_i\}_{i+1}\right]\Delta t \tag{2.21}$$

and

$$\{Q_i\}_{i+1} = \{Q_i\}_i + \Delta t\{\dot{Q}_i\}_i + \left[\left(\frac{1}{2}-\beta\right)\{\ddot{Q}_i\}_i + \beta\{\ddot{Q}_i\}_{i+1}\right]\Delta t^2 \tag{2.22}$$

From Eqs.(2.21) and (2.22), we can obtain $\{\ddot{Q}_i\}_{i+1}$ and $\{\dot{Q}_i\}_{i+1}$ as

$$\{\ddot{Q}_i\}_{i+1} = \frac{1}{\beta\Delta t^2}\left(\{Q_i\}_{i+1} - \{Q_i\}_i\right) - \frac{1}{\beta\Delta t}\{\dot{Q}_i\}_i - \left(\frac{1}{2\beta}-1\right)\{\ddot{Q}_i\}_i \tag{2.23}$$

and

$$\{\dot{Q}_i\}_{i+1} = \frac{\delta}{\beta\Delta t}\left(\{Q_i\}_{i+1} - \{Q_i\}_i\right) + \left(1-\frac{\delta}{\beta}\right)\{\dot{Q}_i\}_i + \left(1-\frac{\delta}{2\beta}\right)\Delta t\{\ddot{Q}_i\}_i \tag{2.24}$$

$[\hat{K}]$ is equivalent stiffness which is also independent of time.

$$[\hat{K}]\{Q_i\}_{i+1} = [\hat{F}]_{i+1} \tag{2.25}$$

While $[\hat{F}]_{i+1}$ is equivalent load vector , which is independent of time,

$$[\hat{K}] = [K] + \frac{1}{\beta\Delta t^2}[M] + \frac{\delta}{\beta\Delta t}[C] \tag{2.26}$$

and

$$\begin{aligned}[\hat{F}]_{i+1} = {} & [F]_{i+1} + [M]\left[\frac{1}{\beta\Delta t^2}\{Q_i\}_i + \frac{1}{\beta\Delta t}\{\dot{Q}_i\}_i + \left(\frac{1}{2\beta}-1\right)\{\ddot{Q}_i\}_i\right] \\ & + C\left[\frac{\delta}{\beta\Delta t}r_i + \left(\frac{\delta}{\beta}-1\right)\dot{r}_i + \frac{\Delta t}{2}\left(\frac{\delta}{\beta}-2\right)\ddot{r}_i\right]\end{aligned} \tag{2.27}$$

All the above equations are included in the main execution code of the Newmark-β method which will be included into the movement program. During the calculation process, it is linked with the solver to obtain the response of cylinders. At the end of each time step, the drag and lift force on the structure will be obtained from the flow solver, and the current position of the centre

of gravity of the cylinder will be updated and its position at the next time step would be obtained. And the grid domain will also be simultaneously updated by a dynamic mesh model. Utilizing rigid motion macro to transfer cylinder's velocity for meshing, when the mesh iteration converged, the whole fluid domain will be updated before the next time-step iteration starts. The loop continues until a stable solution is achieved.

2.4 Boundary conditions

The initial flow conditions grid dimensions are the freestream flow values as presented in Table.1. These corresponding to a Reynolds number of 1500 based on the diameter of the cylinder. The inlet boundary is specified as an velocity inlet boundary with the pressure and temperature specified. The left and right of computational edges in the normal direction will be specified as the symmetric boundary . The internal edges of the oscillating airfoil and moving cylinder are specified as the non-slip wall boundary. The computational outflow boundary is specified as the pressure outlet boundary. The approach that we will take in this study is a 2D LES calculation for a range of values of natural frequencies and damping ratios. The bounded central differencing (BCD) scheme is used for the discretization of the momentum terms. Simple iteration and wall Function are also adopted. The present analysis will focus on calculating the cylinder oscillation and the influence of the natural frequency on the response.

Table.1 Initial condition and grid dimensions

Freestream velocity(m/s)	Reynolds Number	Pressure(Pascal)	Temperature(K)	Angle-of-Attack(deg)	Dimension
1.5	1500	101325	300	0.0	142D×60D

The calculation parameters for the simulations will be chosen as follows. In the present study, we are considering only the case where the diameter of the cylinder equal to the thickness of the oscillating airfoil. So the width of oscillating airfoil (Z) and the diameter of cylinder (D)

are 0.001m, mass ratio (m^*) is 1.67 and 7.85, damping ratio (ξ) is 0.046 and 0.02. The reduced velocity $Vr=U/(f_ND)$ is varied from 2.0 to 9.0 by changing the natural frequency (f_N) of the cylinder. The vibration frequency ratio (f_{so}/f_N) is ranged from 0.37 to 1.667.

As shown in Fig.3(a), the upstream and downstream computational boundary will be respectively set at 20D and 118D away from the round leading edge of the airfoil in the X-direction, while the boundary is set at ±30D in y-direction. An approach based on application of multi-block grids obtained by superimposing different types and scales is adopted which is similar to our previous study[11]. Each grid represents the corresponding element of a hydrodynamic structure of the airfoil and vibrating cylinder flows. As shown in Fig.3(a), the outer Cartesian grid A is in agreement with the calculation domain bounds located sufficiently far from the oscillating airfoil and vibrating cylinder. The deeper black region represents the key computational areas meshed with concentrated grids.

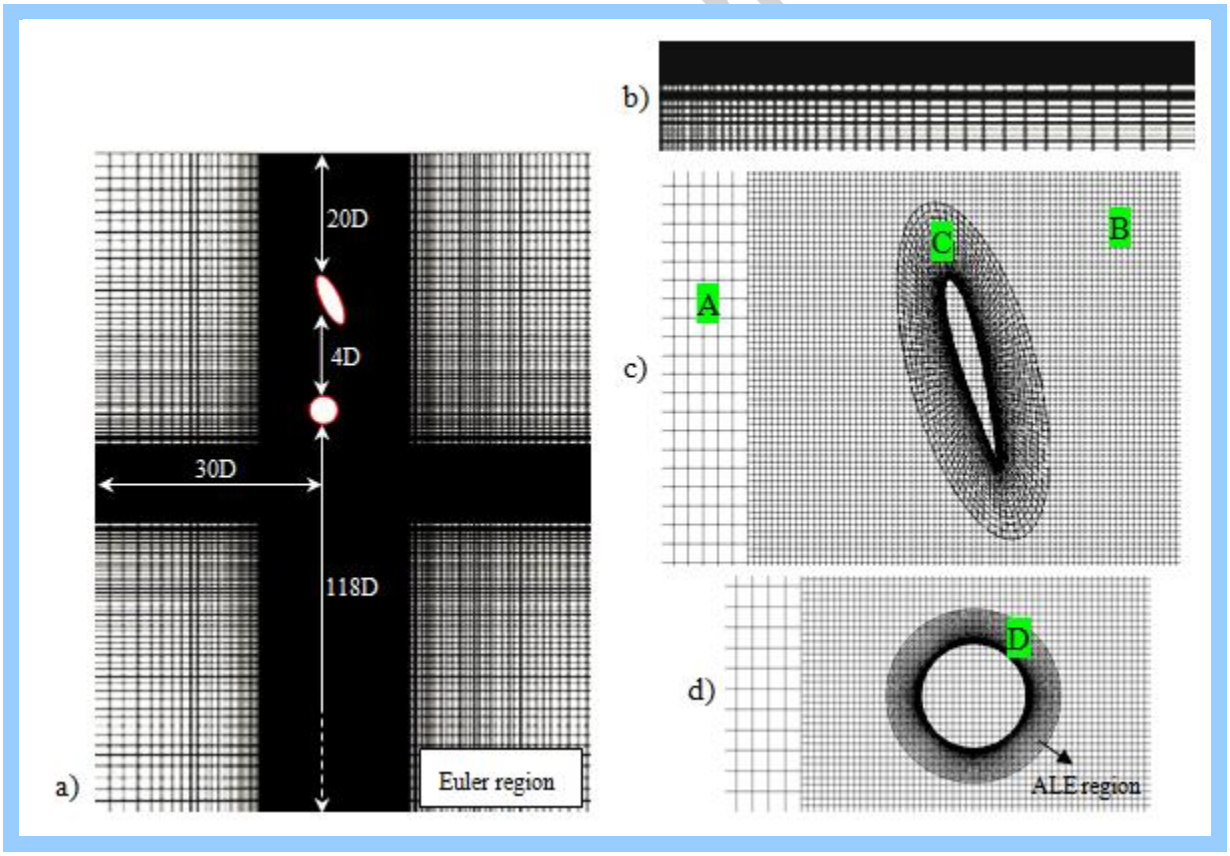

Fig.3 Fragments of the multi-block grid: (a) outer Cartesian grid A; (b) internal Cartesian grid B, representing the far wake representation; (c) Cartesian grids A, B and grid C superimposed in the airfoil area; (d) The finer Cartesian grids D concentrated in the ALE region.

In Fig. 3(b), the unsteady far-field wake between the airfoil and cylinder is represented in detail on the inner Cartesian grid B. A sufficiently fine grid matched with the airfoil and cylinder surface represents comparatively thin boundary and shear layers. Figure 3(c) shows curved grid C superimposed on Cartesian grids A and B at different densities with finer grids concentrating at the regions close to the oscillating airfoil surfaces. Due to the vibration region of the cylinder is relatively smaller comparing with the whole computational region. the Arbitrary Lagrange-Euler (ALE) method in a small region around the cylinder layer (Grid D) will be adopted to generate the whole FSI domain, while other stationary regions will adopt the Euler method. Each time step for the ALE regional grid will be updated simultaneously with the moving cylinder.

3. Validation of the simulated method

3.1 Grid sensitivity test

Estimating precision and errors accumulation is extremely necessary for large simulations of the complex fluid problem. And accumulation of error is proportional to the square rote of the number of time steps. It should be evaluated for each numerical simulation, especially for the unsteady flow state, which has been investigated by Smirnov in details[15-16] The corresponding research have revealed that the relative error of integration in 1D case S_1 is proportional to the mean ratio of cell size ΔL to the computational domain size L_1 in the direction of integration depending on scheme accuracy:

$$S_1 \approx \left(\frac{\Delta L}{L_1} \right)^{k+1} \tag{3.1}$$

As referred by Smirnov[15-16], it can be simplified as: $S_1 \approx (1/N_1)^{k+1}$ in the uniform grid, where N_1 is the number of cells in the direction of integration. k is the order of accuracy of numerical scheme. Then the Eq.3.1 can be summed up as:

$$S_{err} \approx \sum_{i=1}^{2} S_i \tag{3.2}$$

The allowable value of total error $S^{\max}$ can be presumed from 1% to 5%[15-16], then the following inequality should be satisfied as:

$$S_{err} \cdot \sqrt{n} \le S^{\max} \tag{3.3}$$

where n is the number of time steps in Navier-Stokes equations integration. Then the maximum allowable number of time steps can be determined according to the Eq.3.3:

$$n_{\max} = \left(S^{\max} / S_{err}\right)^2 \tag{3.4}$$

The ratio of maximal allowable number of time steps is introduced by Smirnov[15-16], which can be used to characterize the reliability of results. the higher is the value of $n_{\max}$, the lower is the errors.

$$R_s = n_{\max} / n \tag{3.5}$$

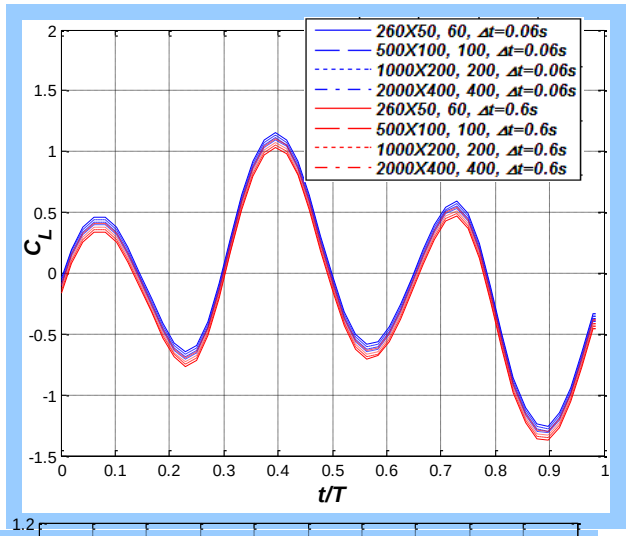

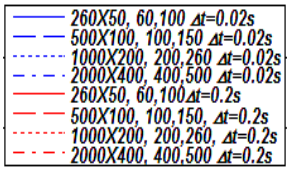

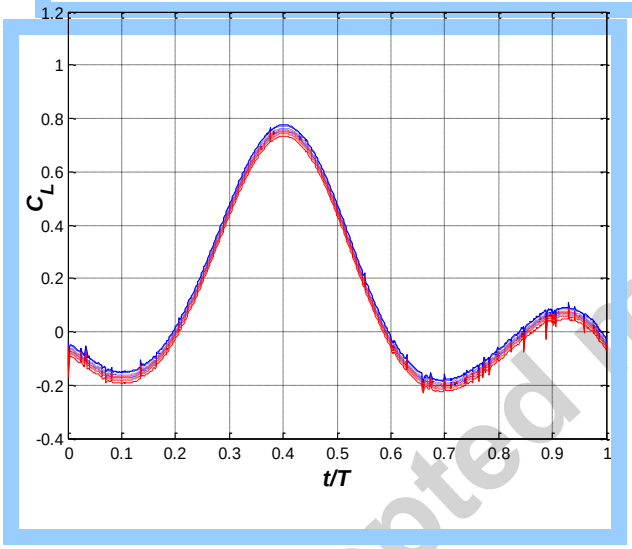

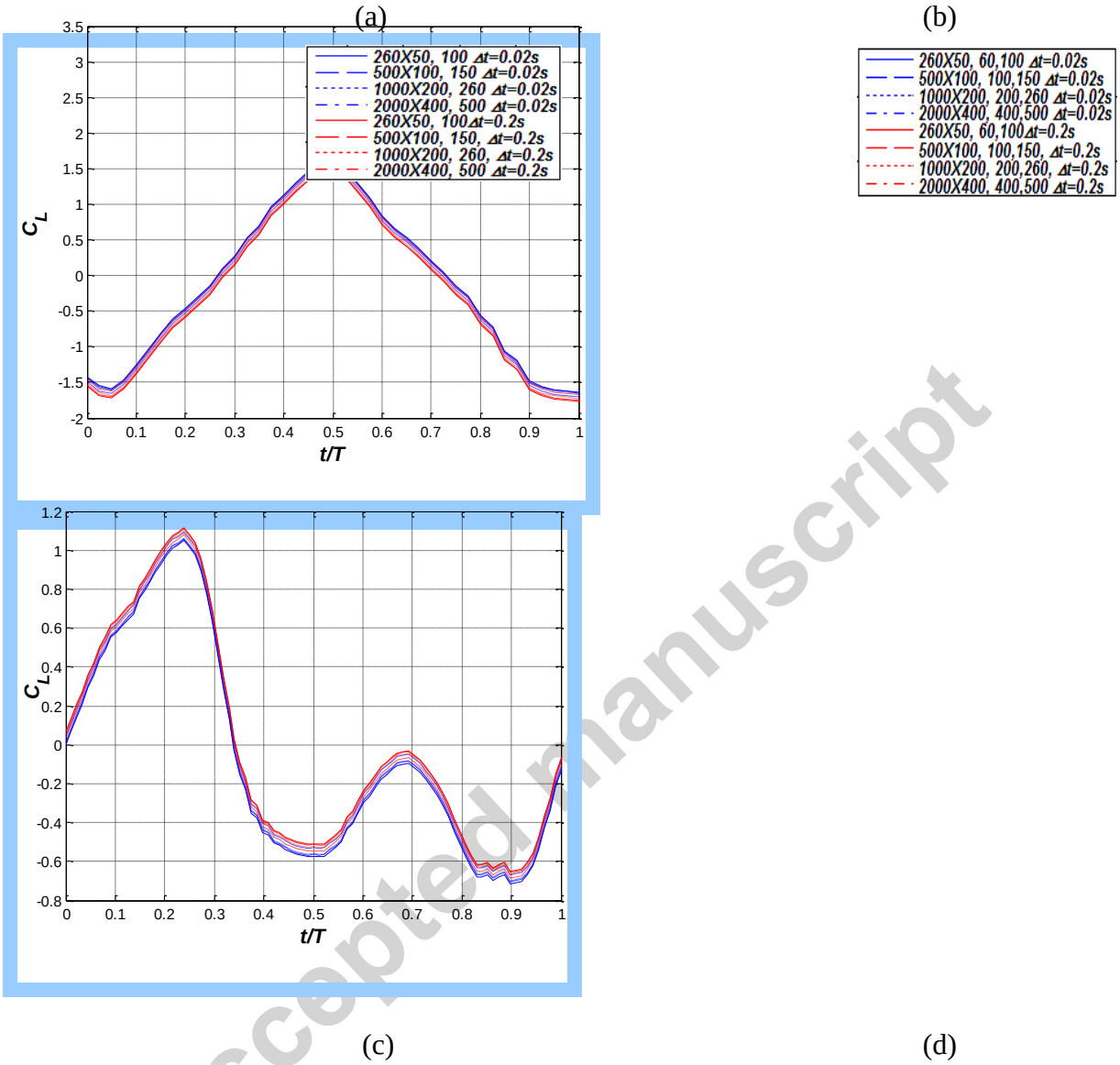

Fig.4 Grid sensitivity test a) a purely oscillating airfoil; b) the oscillating airfoil with a stationary cylinder; c) a single vibrating cylinder under the wake of the free stream; d) the single vibrating cylinder under the wake of the oscillating airfoil case

For this, we have conducted four representative cases in the current research, they are: 1) a purely oscillating airfoil case; 2) the oscillating airfoil with a stationary cylinder; 3) a single vibrating cylinder under the wake of the free stream; 4) the single vibrating cylinder under the wake of the oscillating airfoil case. The grid sensitivity test is performed subsequently, the oscillating airfoil with the "2P" mode wake is chosen and the lift coefficient history at each cycle behind a single cylinder (4D distance) are performed respectively. X stands for the nodes in the

streamwise direction of the computational domain, and Y stands for the nodes in the transverse direction. i and j respectively stands for the nodes on the whole edges of the oscillating airfoil and cylinder. As shown in Fig.4, four different grid sizes ($X \times Y$, i/ j) do not deviate from each other within 5%.

Table.2(a) Error estimate for case01

Allowable error (%)	Grid resolution (X×Y, i)	Physical time simulated (s)	Number of time steps	Accumulated error	Allowable number of time steps	Reliability $R_s=n_{max}/n$
5	260×50, 60	0.06	600	0.000197	$3.85 \cdot 10^{7}$	64167
5	500×100, 100	0.06	1249	0.000036	$2.46 \cdot 10^{9}$	$1.97 \cdot 10^{6}$
5	1000×200, 200	0.06	2728	0.0000066	$1.57 \cdot 10^{11}$	$5.76 \cdot 10^{7}$
5	2000×400, 400	0.06	5661	0.0000012	$1.01 \cdot 10^{13}$	$1.78 \cdot 10^{9}$
5	260×50, 60	0.6	7058	0.000680	$3.85 \cdot 10^{7}$	5454
5	500×100, 100	0.6	12500	0.000113	$2.46 \cdot 10^{9}$	$1.97 \cdot 10^{5}$
5	1000×200, 200	0.6	29998	0.000022	$1.57 \cdot 10^{11}$	$5.23 \cdot 10^{6}$
5	2000×400, 400	0.6	63157	0.000004	$1.01 \cdot 10^{13}$	$1.60 \cdot 10^{8}$

Table.2(b) Error estimate for case02, 03 and 04

Allowable error (%)	Grid resolution (X×Y, j)	Physical time simulated (s)	Number of time steps	Accumulated error	Allowable number of time steps	Reliability $R_s=n_{max}/n$
5	260×50, 100	0.02	400	0.00016	$3.85 \cdot 10^{7}$	96250

5	500×100, 150	0.02	833	0.00003	$2.46 \cdot 10^{9}$	$2.95 \cdot 10^{6}$
5	1000×200, 260	0.02	$1.81 \cdot 10^{3}$	0.000005	$1.57 \cdot 10^{11}$	$8.67 \cdot 10^{7}$
5	2000×400, 500	0.02	$4.02 \cdot 10^{3}$	0.000001	$1.01 \cdot 10^{13}$	$2.51 \cdot 10^{9}$
5	260×50, 100	0.2	$4.23 \cdot 10^{3}$	0.00052	$3.85 \cdot 10^{7}$	9102
5	500×100, 150	0.2	$9.52 \cdot 10^{3}$	0.000098	$2.46 \cdot 10^{9}$	$2.58 \cdot 10^{5}$
5	1000×200, 260	0.2	$2.22 \cdot 10^{4}$	0.000019	$1.57 \cdot 10^{11}$	$7.07 \cdot 10^{6}$
5	2000×400, 500	0.2	$1.53 \cdot 10^{5}$	0.000006	$1.01 \cdot 10^{13}$	$6.6 \cdot 10^{8}$

The detailed analysis for the accumulation of error on different combinations (iteration time step and grid resolution) have also been shown in Table.2(a) and (b). Because the case02, 03 and 04 have shared the same computational domain and iteration time step, therefore the Table.2 has only shown two different phenomena. As shown in Table.2(a) and (b), the accumulation of error for different grid resolution and physical time simulations have been discussed in details. The allowable error is assumed to 5%. The accumulation of error will begin in a fast manner for coarse grid and decreases on the increasing grid resolution and scheme accuracy, but decreases when the physical time increases. This phenomena has also been discussed by Smirnov[15-16]. For present simulations all the results demonstrate high reliability of the used program. but the number of time steps and physical time should not be chosen too large in order to avoiding the accumulation of error in the whole simulation process. Therefore, keeping the certain iteration accuracy and simultaneously avoiding too long simulated period should be the top priority. After the carefully consideration, we will adopt the relatively moderate computation domain size: [1000×200] equipped with i=200 and j=260 nodes in the oscillating airfoil edge and vibrating cylinder circular edge, respectively, in the subsequent computations.

3.2 Comparison of 2D calculated values with 3D and experimental values for stationary cylinder

Table.3 Comparison of 2D calculated values with 3D and experimental values

Re	Cal $\overline{C}_D$ (2D)	Cal $C_{Lr.m.s.}$ (2D)	Cal St (2D)	Cal $\overline{C}_D$ (3D)	Cal $C_{Lr.m.s.}$ (3D)	Cal St (3D)	Exp* $\overline{C}_D$	Exp* St
400	1.212	0.409	0.224	1.208	0.411	0.218	1.2	0.215
1000	1.134	0.391	0.232	1.105	0.408	0.228	1.1	0.22
8000	1.202	0.492	0.228	1.161	0.502	0.221	1.15	0.215
13000	1.18	0.485	0.231	1.192	0.491	0.229.	1.2	0.225

from Lu et al.[17]

As shown in Table.3, the 3D calculated data provided better agreement with experimental data than were obtained for 2D calculations(data from Lu et. al[17]). Indeed 2D calculation is not truly representative of a turbulent flow. However, a 2D calculation does allow for a reasonably accurate estimate of global parameters such as the drag and lift coefficients(shown in Table.3). The negative aspect of the 2D calculation is that the influence of the spanwise wake turbulence is omitted. Transverse oscillation of the cylinder causes the correlation length of the wake vortices to increase which diminishes the 3D influence of vortex shedding, the corresponding behaviors may show some difference between the 2D and 3D calculations. But the 2D approach is not expected to provide a noticeable difference from the actual 3D results once vibration is established. The reason is that the physical fluid motion becomes essentially 2D. Once VIV occurs, the vortices being shed have essentially a 2D structure because of the increased spanwise correlation of the wake vortices when oscillation begins. This also has been proved by Zhang and Dalton[18] who had undertook 2D LES study for a transversely oscillating cylinder at Re=13 000. An amplitude-to-diameter oscillation of about 0.26, with damping ratio of 0.02, was obtained and lock-on was observed to occur from $f$so/f_N of about 1.0 to 1.3. These results showed

the same trends as the experimental results of Feng[19] who undertook one of the first comprehensive experimental studies of this problem.

3.3 1-DOF FSI algorithm validation for the elastically mounted cylinder

Table.4 Cylinder maximum displacement comparisons for m*=1.67 and ζ =0.02

Vr	2.5	3.572	5.554	7.162	10	13.153	16.67	20	22.75
fso/fN	0.555	0.793	1.233	1.59	2.22	2.92	3.7	4.44	5.05
*(y/D)max	0.21	0.418	0.784	0.824	0.873	0.64	0.87	0.71	0.66
+(y/D)max	0.212	0.423	0.773	0.838	0.868	0.648	0.882	0.702	0.657

* Al-Jamal, H. & Dalton, C. (2004)[7]

+ Present

Due to the validation for the single fixed cylinder under the free steady flow has been particularly shown in the previous research[11], now the VIV solutions will be presented by taking the fixed cylinder vortex-shedding frequency f_{so} at fix Reynolds number *Re*, and varying the natural frequency f_N of the cylinder to form the frequency ratio (f_{so} / f_N) so as to verify the FSI solver with the benchmark data. Table.4 shows the maximum dimensionless displacement at several values of f_{so} / f_N with m^*= 1.67 equipped with ξ=0.02. The computational results are showing reasonable overall quantitative agreement with the results from Al-Jamal & Dalton[7], showing the accuracy of the present approach.

4. Vortex shedding interaction between an oscillating airfoil and a fixed cylinder

4.1 Vortex shedding by an oscillating airfoil

The wake regions are labeled using symbols, where "S" signifies a single vortex while "P" signifies a pair of vortices of opposite signs. It is found that oscillating airfoil can generate drag and thrust at certain combination of oscillating frequency (St_D) and amplitude (A_D). The region within $0.1 < St_D < 0.3$ is dominated by the 2S wakes, i.e., von Kármán vortex street at small A_D, and the inverted von Kármán Vortex Street at larger A_D. The part of the phase diagram within $0 < St_D < 0.1$ contains wakes in which more than two vortices are shedded per oscillation period, since the frequency is relatively lower in comparison with the frequency for vortex separation by the side boundary layers. By decreasing St_D or A_D, the 2P pattern would become the 2P+2S wakes, i.e., with a single vortex between vortex pairs. A further decrease in St_D shows the occurrence of the 4P wakes, 4P+2S wakes, and eventually the 8P wakes.

Table.5 Parameters for different oscillation mode generated behind the airfoil[11]

Case	Movement	Wake type	St_D	A_D
C1	Oscillating	Drag von Kármán	0.12	1.14
C2	Oscillating	Thrust inverted von Kármán	0.22	1.81
C3	Oscillating	2P	0.07	1.9
C4	Oscillating	2P+2S	0.04	1.7

In our present simulation, four types of wakes generated by the oscillating airfoil will still be used to study the vortex shedding behind the cylinder and the VIV problem as the previous study. As shown in Table.5, von Kármán drag wake is generated at $St_D = 0.12$ and $A_D = 1.14$.

The inverted von Kármán thrust wake is chosen at $St_D = 0.22$ and $A_D = 1.81$. The 2P wake is at $St_D = 0.07$ and $A_D = 1.9$, and finally the 2P+2S wake is at $St_D = 0.04$ and $A_D = 1.7$.

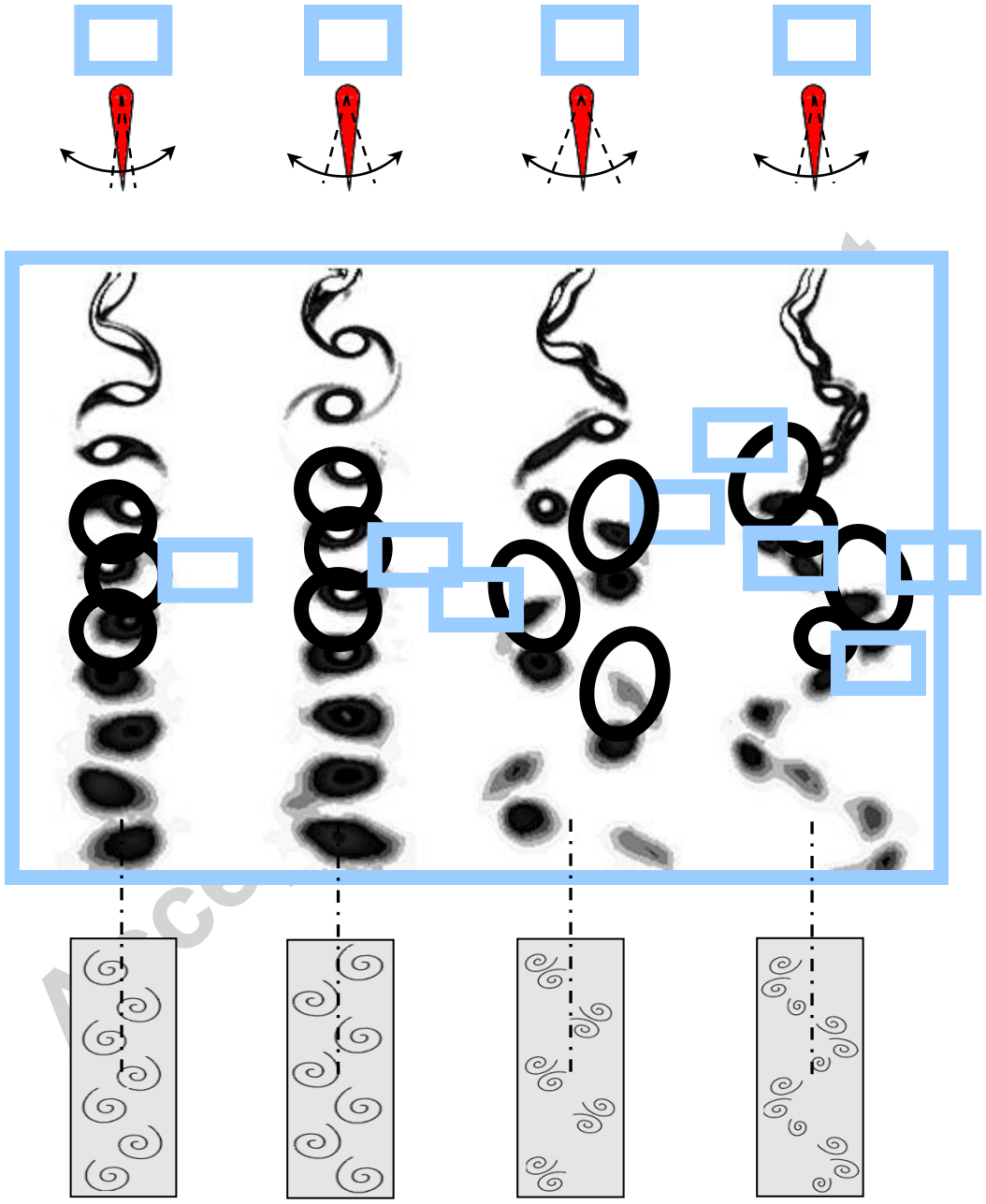

Fig.5 Four types of wakes generated by the oscillating airfoil with different St_D and A_D

(a) Von Kármán wake at $St_D = 0.12$ and $A_D = 1.14$, (b) Inverted von Kármán wake at $St_D = 0.22$ and $A_D = 1.81$, (c) 2P wake at $St_D = 0.07$ and $A_D = 1.9$, (d) 2P+2S wake at $St_D = 0.04$ and $A_D = 1.7$.

In region $0.1 < St_D < 0.3$, drag-producing wakes are found to have velocity profiles showing a momentum deficit when time averaged. As shown in Fig.5(a), the vortex shedding pattern is typically von Kármán vortex street wake configurations with two alternating vortex rows, i.e., clockwise rotary vortices (R.H.S) and anti-clockwise rotary vortices (L.H.S) appeared alternately on either sides of the centerline.

Contrary to the drag-producing wakes, thrust producing wakes shown in Fig.5(b) are always showing a momentum surfeit, superimposed on the momentum-deficit velocity profile in the time-averaged flow. The wake configuration is typically an inverted von Kármán vortex street with two rows of alternating vortices with the anticlockwise ones on the right and the clockwise ones on the left, The above two types of wakes are marked as the "S" type, which mainly occurs in relatively higher oscillating frequencies (*f*) with suitable amplitudes (A).

The transition between these two wake types occurs when the vortices are aligned with the centerline of stream. $0 < St_D < 0.1$ contains the wakes in which more than two vortices are shedded per oscillation cycle due to the fact that the oscillating frequency is relatively low in comparison with the frequency for vortex separation in the side boundary layers. As shown in Fig.5(c), two pairs of vortices with comparable strength are formed and are moving gradually away from the centerline. On the L.H.S, the anticlockwise vortex (left-top) pairs with the clockwise vortex (right-bottom), while on the R.H.S, the clockwise vortex (right-top) pair with the anticlockwise vortex (left-bottom). By decreasing St_D or A_D, the 2P wakes will transform into the 2P+2S wakes (see Figs.5(d)), with a single vortex appeared between the vortex pairs, the vortices are more closely connected with one another. Contrary to the 2P wake, the anticlockwise

vortex (right-top) pairs with the clockwise vortex (left-bottom) appear on the L.H.S, while on the R.H.S, the clockwise vortex (left-top) pairs with the anticlockwise vortex (right-bottom).

4.2 Vortex shedding for the fixed cylinder in the wake of the oscillating airfoil

When the cylinder is introduced into the wake of the oscillating airfoil, the vortex shedding behind the airfoil maintains the same Strouhal numbers but has shown different flow patterns. As shown in Fig.6(a) and for the drag-producing von Karman vortex wake, the presence of the cylinder has little effect on the flow patterns of the "2S" mode comparing to a single oscillating airfoil (compare Fig.5(a)). The vortices shedded from the boundary layers of the oscillating airfoil will interference with the vortices created by the cylinder and then merged to form two alternating concentrated vortex rows. For the thrust-producing case, the vortex shedding has become totally different from that of previous pure oscillating airfoil ("2S" mode). As shown in Fig.6(b), the "2S" mode has changed into the "P+S" mode, i.e., a pair of vortices located on the L.H.S of the centerline, with another isolated single vortex located on the R.H.S. The distance between the vortex pair and single vortex will be shortened gradually at downstream locations. Decreasing the oscillating frequency further, the "2P" wakes appear again. However, this type of "2P" mode is not the same as that found in the pure oscillating airfoil (Comparing Fig.6(c) with Fig.5(c)). In the pure oscillating airfoil case, the pair of vortices are longitudinal parallel to each other and both vortices within a pair are approximately equal in strength. When adding the cylinder into the wake, the pairs of vortices have become laterally parallel to each other. The two pair vortices have also shown different sizes and strength. The stronger vortices are located closer to the centerline than the weaker ones.

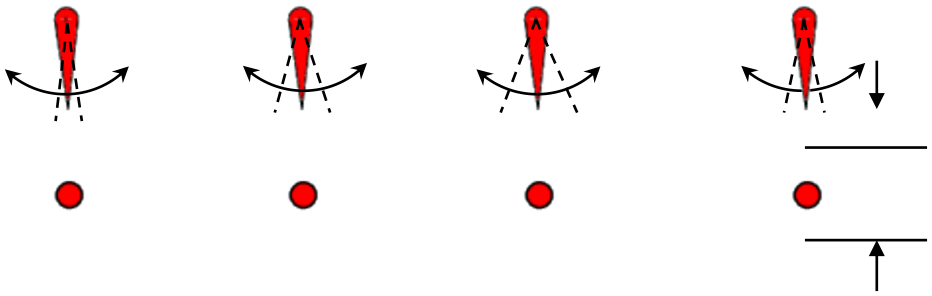

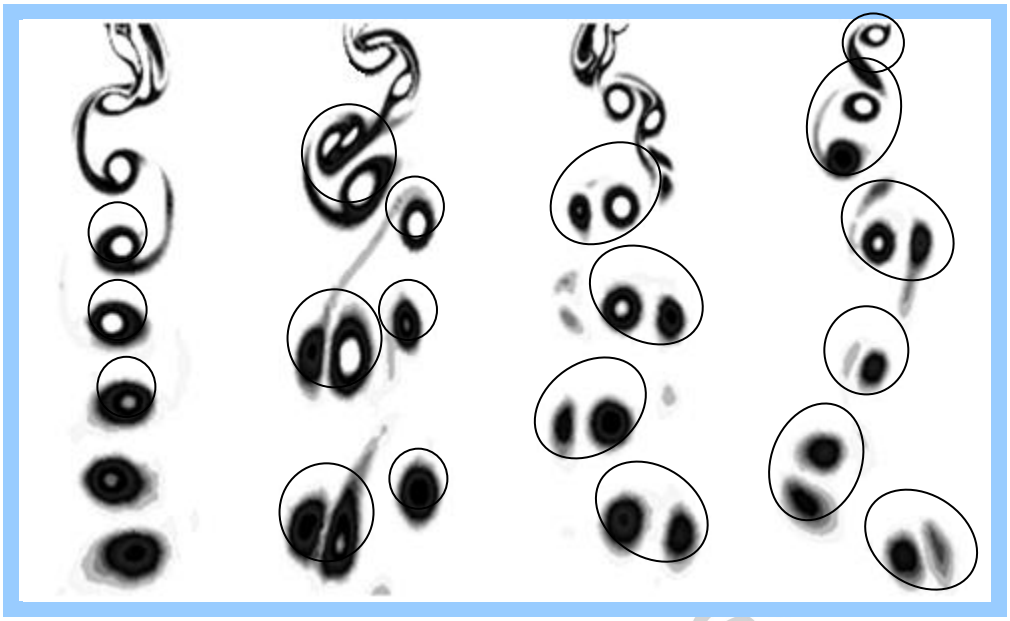

Fig.6 Vortex shedding for the fixed cylinder in the wake of the oscillating airfoil: (a) Von Kármán drag wake, (b) Inverted von Kármán thrust wake, (c) 2P wake, (d) 2P+2S wake.

As shown in Fig.6(d), the vortex shedding has also been changed due to the presence of the cylinder. Different from that of the pure oscillating airfoil (compare Fig.5(d)), the shedded vortices from the oscillating airfoil are merged with the vortices generated by the cylinder wake. The merged single vortices do not appear between the vortices pairs, but rather they emerge after every two pairs of vortices.

5. 1-DOF Vortex Induced Vibration (VIV)

5.1 Induced by the steady flow

When the circular cylinder is flexibly mounted with low damping and reduced mass, vortex induced vibration can occur. Once the oscillation starts, the downstream flow will be totally changed and the responses of the affected cylinder will also feedback onto the fluid. The VIV solutions will be presented by taking the fixed cylinder vortex-shedding frequency f_{so} at a fixed Reynolds number. The frequency ratio (f_{so} / f_N) is formed by varying the natural frequency f_N of the cylinder so as to verify the FSI solver with the benchmark data. Here *y* represents the vibrating amplitude with respect to the cylinder. In this section, the numerical simulation of 1-

DOF-VIV for an isolated elastically mounted cylinder under steady flow will be reported so as to establish the basis for analyzing the VIV of the cylinder induced by different types of oscillating airfoil motion. The solutions will be presented by varying the natural frequency f_N of the cylinder so as to create the frequency ratio (f_{so}/f_N) and reduced velocity V_r. By varying V_r in an increment of one (starting from V_r=2 to 16), the lock-in region can be determined. The calculated response curve (vibration amplitude against reduced velocities) is shown in Fig.7.

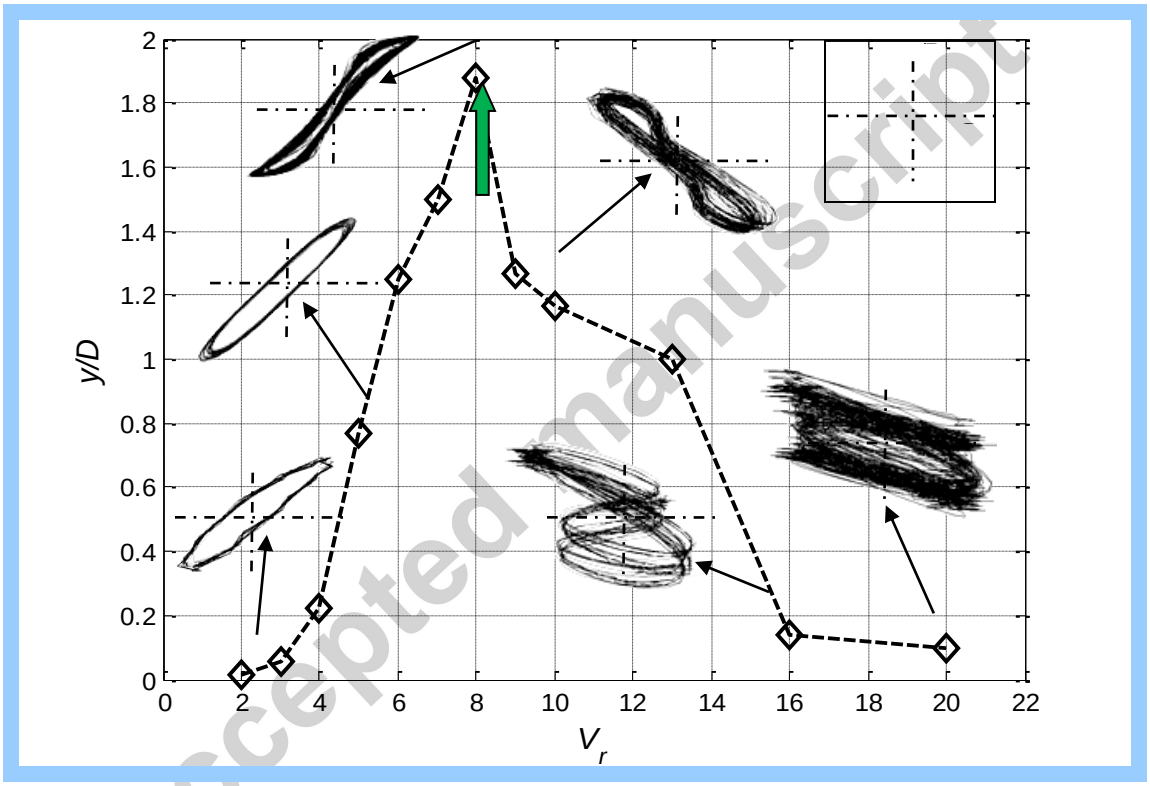

Fig.7 The calculated response curve (maximum vibration amplitude *vs* reduced velocities) for an isolated cylinder (m^*=1.67, ξ=0.02)

The peak oscillation amplitude occurs at $f_{so}/f_N = 0.675$ which corresponds to a reduced velocity of about 8. The curve falls off to smaller values at the extremes of the frequency ratio range $0.27 \le f_{so}/f_N \le 2.7$. The oscillation amplitude is obviously reduced at a lower reduced velocity (V_r=16). When the calculated response curves are imposed onto a Cartesian coordinate system, it can be seen that before V_r=8, all the phase portraits occupy mainly in the first and third quadrants, and the lift coefficients and displacement are in-phase. As the reduced velocity

increases, the phase portrait will begin to rotate counterclockwise, and after V_r =9, the corresponding phase portraits will appear in the second and fourth quadrants, and the lift coefficients and displacements become out of phase.

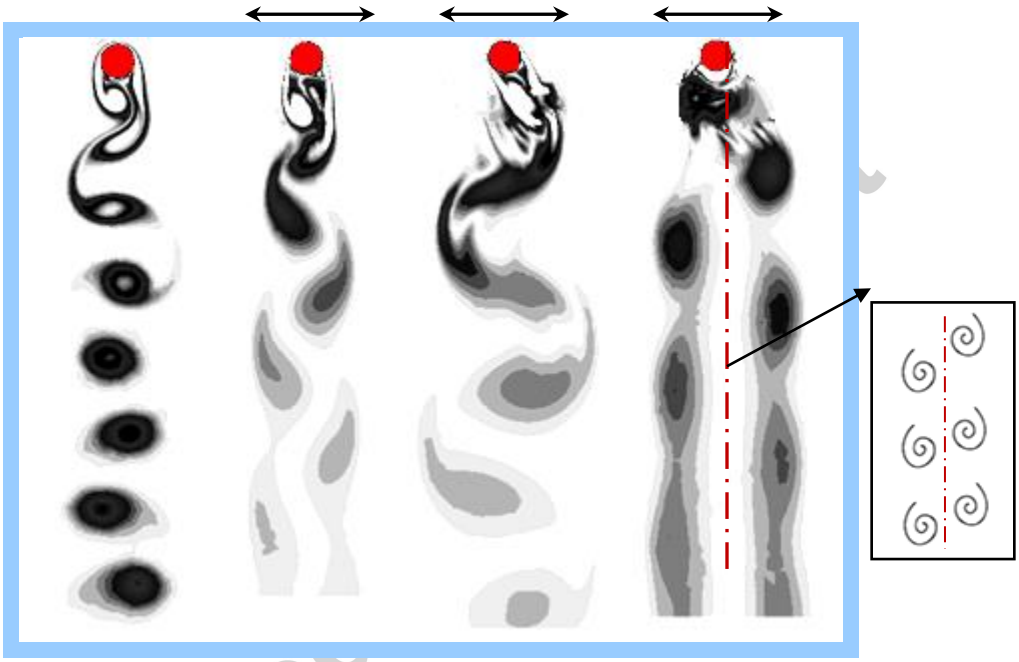

Fig.8 Vortex shedding for the 1-DOF-VIV of a single cylinder under steady flow:

(a) fixed, (b) V_r =3, (c) V_r =8, (d) V_r =12

As shown in Fig.8(a) and for a fixed cylinder, the vortex shedding shows alternately regular "2S" mode. At V_r =3, the vortices will be affected by the transverse vibration of the cylinder, the bandwidth of vortices becomes larger than the fixed case (see Fig.8(b)). Two adjacent vortices with opposite direction become closer to each other. For the V_r =8 case in Fig.8(c), the bandwidth of vortices has developed to the maximum. By V_r =12 (see Fig.8(d), the shedded vortices have formed two parallel vortex streets on either sides of the centerline.

5.2 Induced by the oscillating airfoil

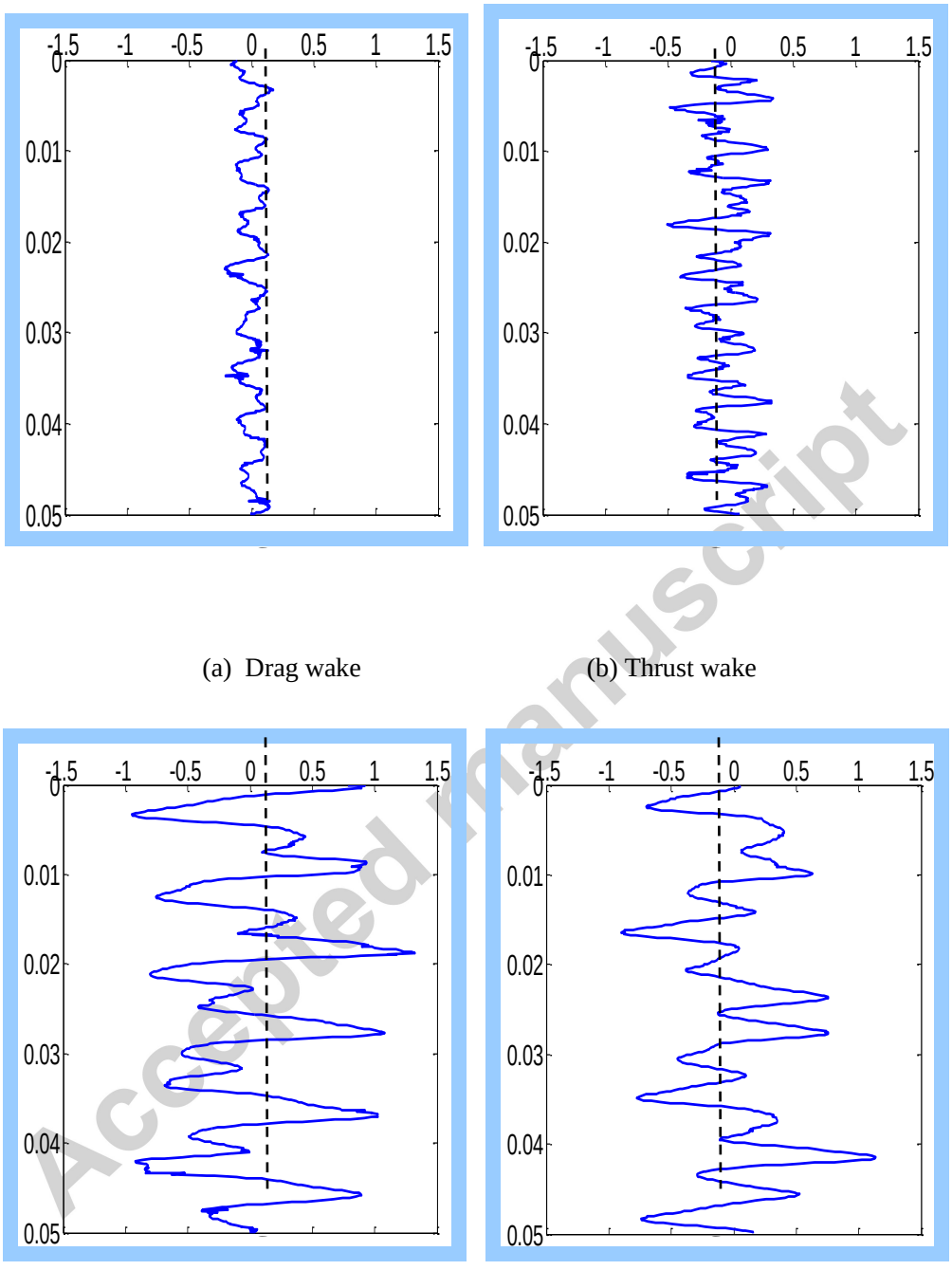

(a) Drag wake (b) Thrust wake

(c) 2P wake (d) 2P+2S wake

Fig.9 Lift coefficients for a vibrating cylinder (1-DOF) behind the wake of an oscillating airfoil.

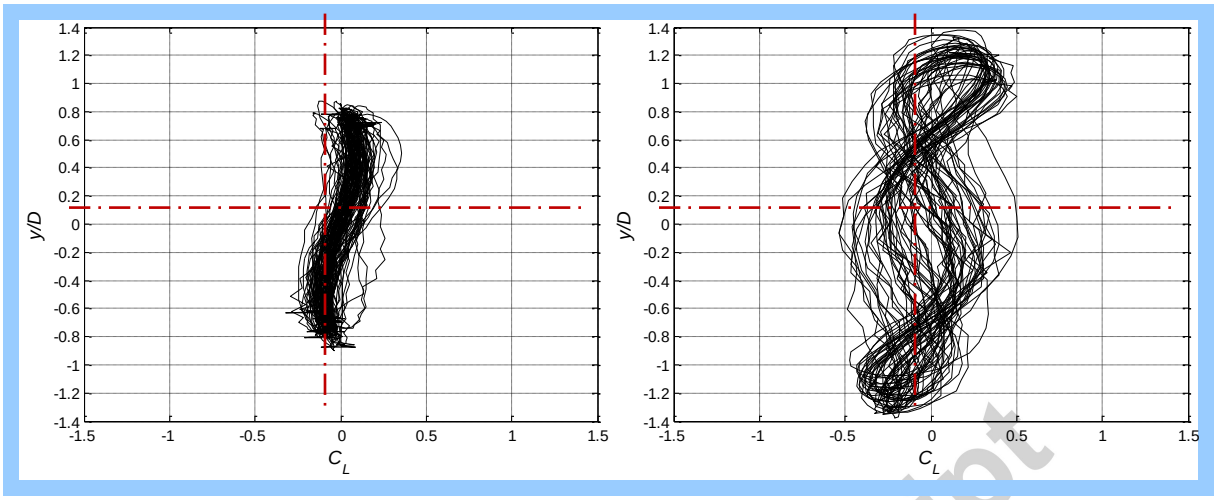

(a) Von Kármán drag wake

(b) Inverted von Kármán thrust wake

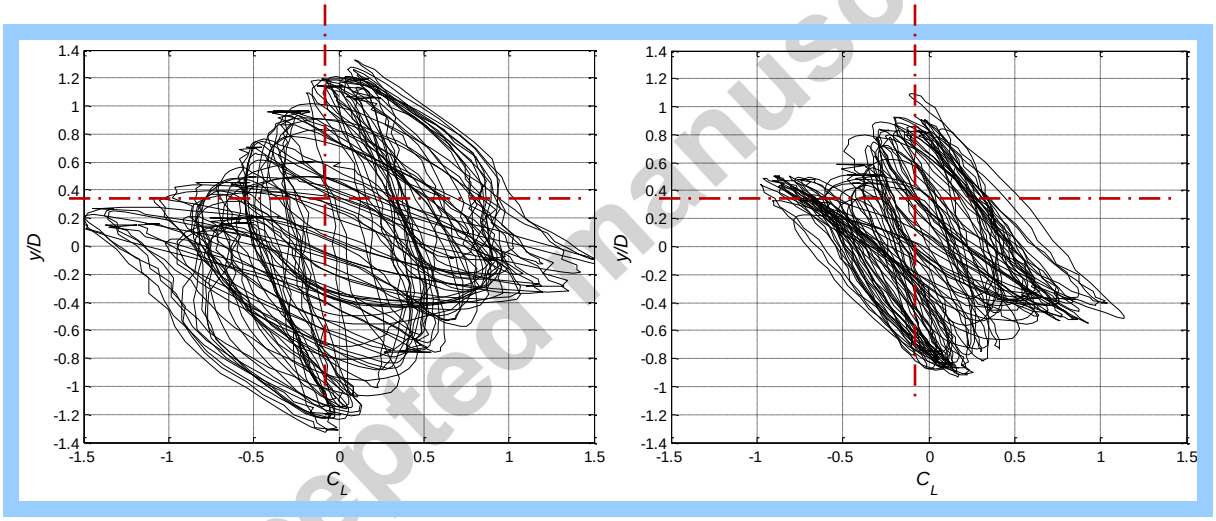

(c) 2P wake

(d) 2P+2S wake

Fig.10 Phase portraits of displacements *vs* lift coefficients (1-DOF) at different wakes of an oscillating airfoil for the isolated cylinder (m^*=1.67, ξ=0.02).

Fig.9 shows the lift characteristics for a vibrating cylinder (1-DOF) behind the wake of an oscillating airfoil. From drag wake (Fig.9(a)) to 2P+2S wake (Fig.9(d)), the oscillating frequency is decreasing gradually and the period of vortex shedding is also extended gradually, as may have been expected. To further investigate the 1-DOF vibration induced by the different motions of oscillating airfoil, the phase portraits of displacements *vs* lift coefficients (1-DOF) at different wakes of the oscillating airfoil for an isolated cylinder (m^*=1.67, ξ=0.02) are plotted in Fig.10.

There are several new and important features with respect to the phase portraits. For all the cases considered, the corresponding phase portraits are almost symmetrical with respect to the coordinate system. Firstly, for the vibration induced by the von Kármán drag wake case (shown in Fig.10 (a)), the phase portraits of displacements mainly show a series of the single bending curves. For the inverted von Kármán thrust wake case shown in Fig.10(b), the phase portraits have been changed to a single closed orbit (double "8-shape" like). The corresponding lift coefficients for these two cases are also showing relatively smaller magnitudes than that of the 2P and 2P+2S wakes (comparing Figs.10(c) and (d)). For the 2P and 2P+2S cases, the flow becomes more complex in the vortex shedding process behind the elastic cylinder, the phase portraits of displacements are showing a quasi-periodic pattern instead of a single closed orbit. Comparing with the 2P+2S wake, the 2P wake has shown relatively higher transverse vibration amplitude and lift coefficient.

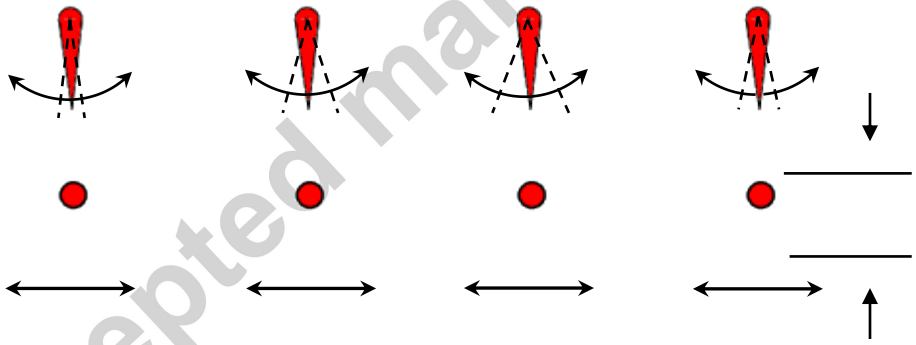

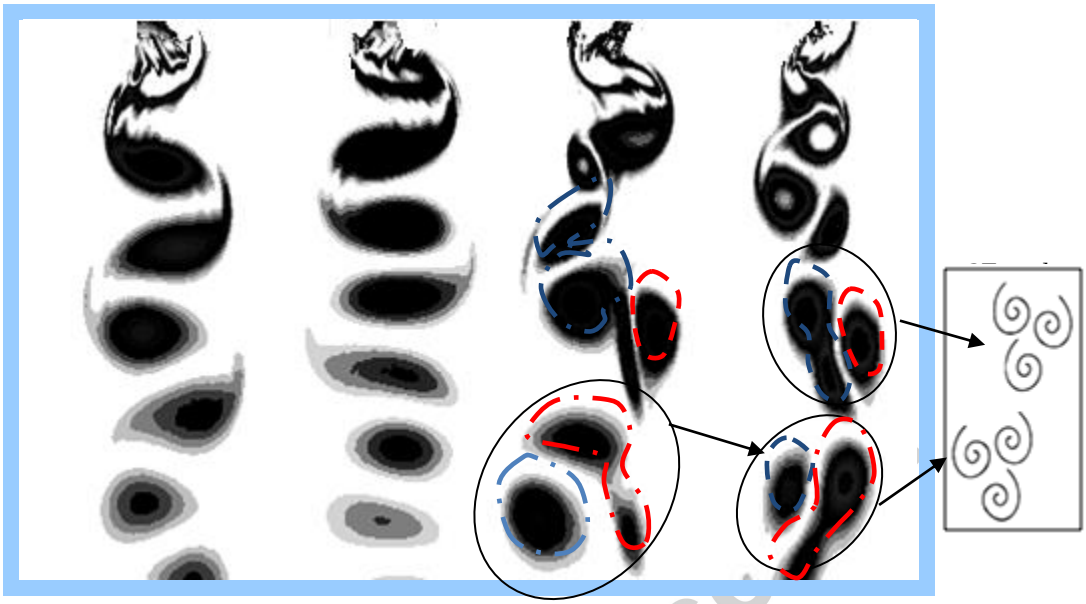

Fig.11 Vortex shedding for the 1-DOF-VIV of cylinder in different wakes of the oscillating airfoil: (a) Von Kármán drag wake, (b) Inverted von Kármán thrust wake, (c) 2P wake, (d) 2P+2S wake

Fig.11 shows the vortex shedding for the 1-DOF VIV of cylinder at different wakes of the oscillating airfoil. For the von Kármán drag oscillating case (see Fig.11(a)), the corresponding vortex shedding pattern still maintains the typical "2S" mode, i.e., clockwise (R.H.S) and anti-clockwise (L.H.S) appeared alternately on either sides of the centerline. For the thrust-producing oscillating case, the vortex shedding has become different from that of previous fixed case (Fig.6(b), "P+S" mode). It has changed back into the typical thrust-producing wake like the vortex shedding behind the single oscillating airfoil (comparing Fig.11(b)), The wake configuration is typically an inverted von Kármán vortex street with two rows of alternating vortices. For the "2P" oscillating case shown in Fig.11(c), we also find two triplets of vortices at each oscillating cycle ("2T" mode), which was firstly observed experimentally by Jauvtis and Williamson[20]. As the flow moves downstream, this mode will vanish gradually. For the "2P+2S" oscillating case shown in Fig.11(d), the "2T" mode can be observed more clearly, and the strength are also stronger than that of "2P" oscillating case.

5.3 Vortex structure comparison for the different configurations and motions

Fig.12 shows the wake formation features at different configurations, i.e. a) fixed cylinder under the steady flow; b) fixed cylinder under the 2P wake of the oscillating airfoil; c) 1-DOF (Y-only) vibrating cylinder behind the 2P wake of the oscillating airfoil.

For the fixed cylinder under the steady flow case (shown in Fig.12(a)), the regular vortex shedding pattern has been observed, i.e. two alternating vortex rows clockwise right (B) and anti-clockwise left (A) for a flow from top to bottom. Two types of vortices structure are also more concentrated and enlaced with each other. Due to the fact that the cylinder is fixed and the symmetrical vortex shedding would cause the fluctuation of lift coefficient to be stable with the same peak value (C_{lmax}=0.85) at every cycle.

For the fixed cylinder under the 2P wake of the oscillating airfoil case (shown in Fig.12(b)), the vortices P1 and P2 are formed from the oscillating airfoil motion ($St_D = 0.07$ and $A_D = 1.9$) upstream, and the cylinder will generate secondary vortices (marked as A and B). When they arrive at the cylinder, P1 will merge with B4 forming a new clockwise vortex (B3). P2 will also merge with A4 to form a new anti-clockwise vortex (A3). This phenomenon will repeat in cycle. As a result, the "2P" vortices mode can still be maintained. However, comparing with the "2P" mode generated by the pure oscillating airfoil, the pairs of vortices have become lateral parallel to each other. The two pair vortices have also shown different sizes and strength. The stronger vortices are mainly near the centerline of the stream. The corresponding lift coefficient has also shown the regular beating phenomenon with two peak values at every cycle.

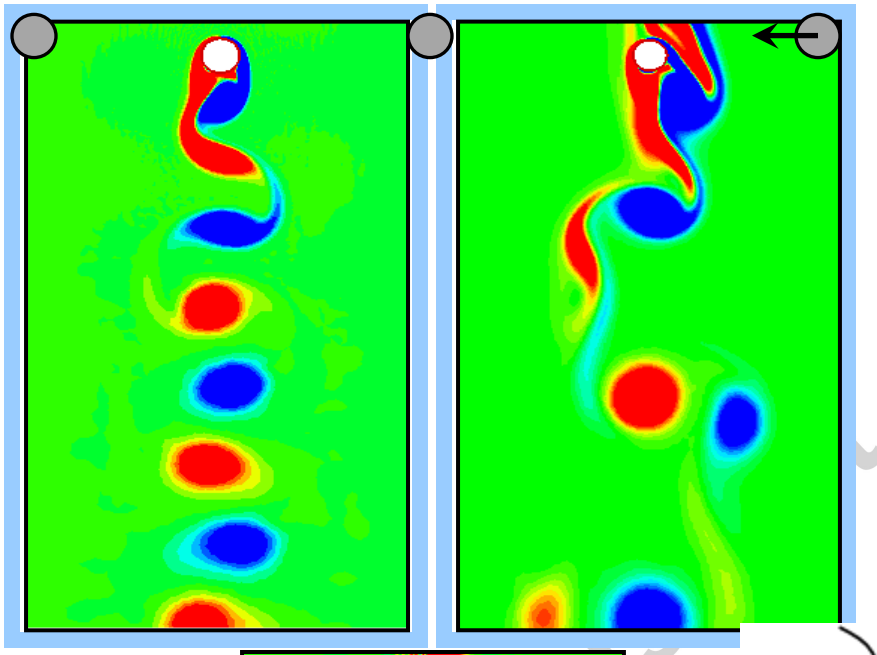

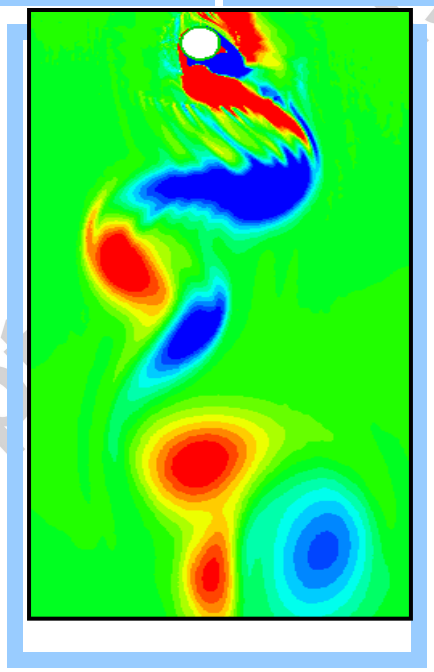

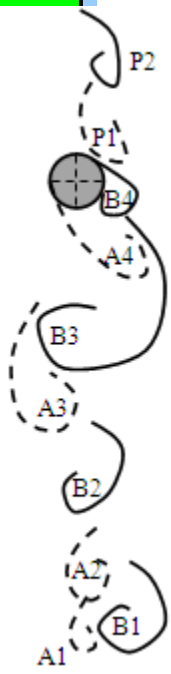
P2
P1
B4
A4
B3
A3
B2
A2
B1
A1

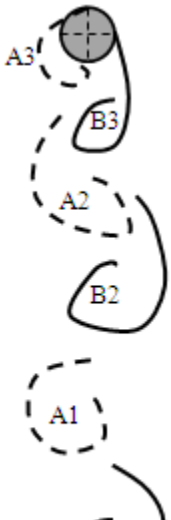
A3
B3
A2
B2
A1

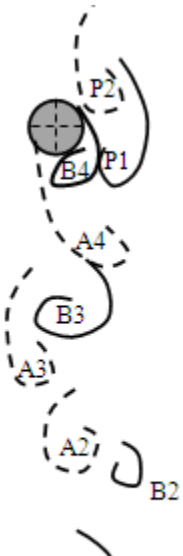
P2
B4
P1
A4
B3
A3
A2
B2

(a) (b) (c)

Fig.12 Votex formation patterns under different types of wakes (Dashed line: anti-clockwise; Solid line: clockwise) a) Fixed cylinder under steady flow; b) Fixed cylinder under the influence of the oscillating airfoil; c) 1-DOF under the influence of the oscillating airfoil.

For the 1-DOF vibrating cylinder under the 2P wake of the oscillating airfoil case (Fig.12(c)), due to the fact that the cylinder can now move in the lateral direction (Y-only), the affected region will be enlarged. When the cylinder is moving to the left, the newly generated vortices A4 and B4 would be shifted to the R.H.S of the centerline. In the subsequent downstream position, a triplet of vortices composed of A1, A2 and B1 is forming gradually. This type of vortices has been defined as "2T" mode by Jauvtis and Williamson[20]. This triplet strongly resembles the vortex pairs (A1-B1 and A3-B2) formed at each half-cycle in the 2P mode, with an addition of the third vortices (A2 and B3) formed during the acceleration phase near the extremities of the transverse motion. At further downstream position, the vortices A1, A2 and B1 have formed a typical "2T" mode. Due to the motion of cylinder and relatively complex vortex shedding, the lift coefficient is also showing quite irregular beating phenomenon.

6 Concluding Remarks

For the single degree of freedom vortex induced vibration in the wake of the free stream, the oscillation amplitude is obviously reduced at a lower reduced velocity. Putting the calculated response curves into a Cartesian coordinate system, it can be observed that when the value of the reduced velocity increases less than 8, all the phase portraits occupy in the first and third quadrants, and the lift coefficients and displacement are in-phase. As the reduced velocity further increased, the phase portrait will begin to rotate counterclockwise from the first and third quadrants to the second and fourth quadrants in a Cartesian coordinate system.

When the cylinder is positioned in the wake of the oscillating airfoil, for the vibration induced by the von Kármán drag wake case, the phase portraits for displacements show a series of the single bending curves. For the inverted von Kármán thrust wake case, the phase portraits of displacements have been changed to a single closed orbit (double "8-shape"). The corresponding lift coefficients for these two cases are showing the relatively smaller magnitudes than that of the pair and single plus pair wakes. The phase portraits of displacements are also displayed more regularly in the vortex shedding process. For the pair and single plus pair wakes, the phase portraits for the displacements become more complex. Comparing with the single plus pair wakes, the pair wake shows relatively higher transverse vibration amplitudes and lift coefficients.

For the vortex shedding in the single degree of freedom vortex induced vibration case at the different wakes of the oscillating airfoil, the vortices shedded from the oscillating airfoil boundary layers will be mixed with the vortices created by the vibrating cylinder and generate concentrated vortices in both the drag and thrust producing cases. For the pair and single plus pair oscillating cases, two triplets of vortices per cycle are formed. As the flow moving downstream, this mode will vanish eventually.

Acknowledgments

Financial support from National Science Foundation of China [Grant number 11602023] is gratefully acknowledged. The authors also would like to thank the reviewers for their helpful suggestions.

References

[1] Y. Qiu, Y. Sun, Y. Wu, and Y. Tamura, Effects of splitter plates and Reynolds number on the aerodynamic loads acting on a circular cylinder, J. Wind Eng. Ind. Aerodyn. 2014(127), 40-50.

[2] F. Gu, J. S. Wang, X. Q. Qiao, and Z. Huang, Pressure distribution, fluctuating forces and vortex shedding behavior of circular cylinder with rotatable splitter plates, J. Fluids Struct. 2012(28), 263-278.

[3] M. Zhao, L. Cheng, and L. Lu, Vortex induced vibrations of a rotating circular cylinder at low Reynolds number, Phys. Fluids. 2014(26), 477-539.

[4] L. Lu, X.L. Guo, G.Q. Tang, M.M. Liu, C. Q. Chen, Z. H. Xie, Numerical investigation of flow-induced rotary oscillation of circular cylinder with rigid splitter plate. Physics of Fluids, 2016(28), 124-150.

[5] S.C. Hsieh, Y.M. Low, Y.M. Chiew, Flow characteristics around a circular cylinder subjected to vortex-induced vibration near a plane boundary. J. Fluids Struct., 2016(65), 257-277.

[6] T. Schnipper, A. Andersen, T. Bohr, Vortex wakes of a flapping airfoil. J. Fluid Mech., 2009(633), 411-423.

[7] H. Al-Jamal, C. Dalton, Vortex induced vibrations using Large Eddy Simulation at a moderate Reynolds number. J. Fluids Struct., 2004(19), 73-92.

[8] C.H.K. Williamson, R. Govardhan, Vortex-induced vibrations. Annu. Rev. Fluid Mech., 2004(36), 413.

[9] I. Borazjani, F. Sotiropoulos, Vortex-induced vibrations of two cylinders in tandem arrangement in the proximity–wake interference region. J. Fluid Mech., 2008(211), 1541–1558.

[10] T. Sarpkaya, A critical review of the intrinsic nature of vortex-induced vibrations. J. Fluids Struct., 2004(19), 389.

[11] G.Q. Zhang, L.C. Ji, Investigation of two degrees of freedom on vortex-induced vibration under the wake interference of an oscillating airfoil. Acta Astronautica, 2016. (online)

[12] L. Wen, T.M. Wang, G.H. Wu, J. H. Liang, Hydrodynamic investigation of a self-propelled robotic fish based on a force-feedback control method. Bioinspiration & Biomimetics, 2012(7), 1-17.

[13] D.R. Godoy, J.L. Aider, J.E. Wesfreid, Transitions in the wake of a flapping foil. Physical Review E – Statistical, Nonlinear, and Soft Matter Physics, 2008(77), 1-6.

[14] Y.A. Dynnikov, G.Y. Dynnikova, S.V. Guvernyuk, Simulation of the flexible body moving in viscous fluid. Proceedings of the ECCOMAS Thematic Conference on Multibody Dynamics 2015. International Center for Numerical Methods in Engineering. Barcelona, Catalonia, Spain, 2015. 960–967.

[15] N.N. Smirnov, V.B. Betelin, V.F. Nikitin, L.I. Stamov, D.I. Altoukhov. Accumulation of errors in numerical of chemically reacting gas dynamics. Acta Astronautica, 2015(117), 338-355.

[16] N.N. Smirnov, V.B. Betelin, R.M. Shagaliev, V.F. Nikitin, I.M. Belyakov, Yu.N. Deryuguin, S.V. Aksenov, D.A. Korchazhkin. Hydrogen fuel rocket engines simulation using LOGOS code. International Journal of Hydrogen Energy, 2014(39), 10748-10756.

[17] X. Lu, C. Dalton, and J. Zhang. Application of Large Eddy Simulation to flow past a circular cylinder, ASME J. Offshore Mechanics and Arctic Engineering, 1997(119), 519-525.

[18] J. Zhang, C. Dalton. Interaction of vortex-induced vibrations of a circular cylinder and a steady approach flow at a Reynolds number of 13,000. Computers and Fluids, 1996(25), 283-294.

[19] C.C. Feng. The measurement of vortex-induced effects in flow past stationary and oscillating circular and D-section cylinders. M.A.Sc. Thesis, University of British Columbia, Vancouver, 1968.

[20] N. Jauvtis, C.H.K. Williamson, The effect of two degrees of freedom on vortex-induced vibration at low mass and damping. J. Fluid Mech. 509 (2004), 23-62.

Highlights

- Phase portraits (1-DOF) will rotate counterclockwise in Cartesian coordinate.

- Single bending and double “8-shape” are newly found in displacement curves.
- The “2T” vortices mode have been newly found in 2P and 2P+2S vortex wakes.